Estuarine, Coastal and Shelf Science 215 (2018) 39–51

Contents lists available at ScienceDirect

Estuarine, Coastal and Shelf Science

journal homepage: www.elsevier.com/locate/ecss

Numerical study on factors influencing typhoon-induced storm surge distribution in Zhanjiang Harbor

Xing Liu[a,c], Wensheng Jiang[a,b,*], Bo Yang[a], John Baugh[c]

[a] Physical Oceanography Laboratory/CIMST, Ocean University of China and Qingdao National Laboratory for Marine Science and Technology, Qingdao, Shandong, 266100, PR China

[b] Laboratory of Marine Environment and Ecology (Ministry of Education of China), Ocean University of China, Qingdao, Shandong, 266100, PR China

[c] Department of Civil, Construction, and Environmental Engineering, North Carolina State University, Raleigh, NC, 27695, United States

ARTICLE INFO

Keywords:
Local atmospheric effect
Remote atmospheric effect
Storm surge
Spatial distribution
Sea level rise
Typhoon track

ABSTRACT

A 2-D unstructured finite element model is used to study how local and remote atmospheric forcing, sea level rise, and shoreline variation affect typhoon-induced storm surge in a small shallow bay, Zhanjiang Harbor (ZH). In this research, the spatial distribution of storm surge is divided into three patterns in ZH, denoted E-W, N-S, and S-N, using a quantitative method. In the Bay, local atmospheric effects (LAE) and remote atmospheric effects (RAE) both play important roles in the maximum residual water level. The contribution of RAE to the inflow is higher than that of the LAE, but the former is less important in the spatial distribution in ZH. In addition, the typhoon track influences the time of occurrence of the maximum surge by forcing the outer waters to ZH, then the spatial distribution of the surge residual in the bay is controlled by local winds, and different regions are threatened during different kinds of storm surge processes. Two sea level rise scenarios are set up in the paper as well, and the results show that the trends of the changes in LAE and RAE in the inner-bay are the opposite in the case of sea level rise; however, the total changes of the distribution are not the same in different categories. In general, the E-W category storm surge is weakened, while the N-S and S-N category storm surges have inverse changes in the north and south of ZH. There is a downward trend of the maximum surge gradient within the Bay, but relative to sea level rise itself this effect is not obvious. The establishment of the sea embankment increased the storm surge within the bay though it is not significant.

1. Introduction

Zhanjiang Harbor (ZH), located at the northwestern tip of Leizhou Peninsula and shaped like a letter “T” on the southern coast of Guangdong Province, China, is a semi-enclosed bay with a 40 km-long main channel (Fig. 1). It is surrounded by Nansan Island, Donghai Island, and Leizhou Peninsula. There are numerous ports, communities, and natural villages distributed in the coastal region of ZH that are vulnerable to the effects of tropical cyclones. According to Chen et al. (2002), the number of the tropical cyclones affecting ZH is greater than 6 annually on average, accounting for more than 40% of the number of tropical cyclones entering the South China Sea. More than 50% of the tropical cyclones affecting ZH are typhoons (Chen et al., 2002). When tropical cyclones come from the east, ZH usually acts like the bottom of a bag, collecting a huge amount of water; hence it is one of the areas in China most vulnerable to typhoon events (Chen et al., 2002;; Jiang et al., 2003; Zhang et al., 2009).

The coastal area of ZH is complex with large, scattered, and distributed intertidal zones, and the coastline of ZH is rugged and rough. Before the 1960s there were 3 tidal channels around ZH, but in February 1961 a levee called the Lanhai levee was built between Donghai Island and the mainland so that the water exchange through this channel was cut off (Ying and Wang, 1996). Thus there are only 2 channels left at present, the Nansan River and the Dahuang River, located along the north and south side of Nansan Island respectively. The water depth is less than 5 m throughout most of the Nansan River, which is relatively shallow. The water depth in most areas of the Dahuang River ranges from 10 to 20 m, and the depth of the deepest area is more than 30 m (Fig. 1).

ZH is mainly dominated by the irregular semidiurnal tides (Ding, 1986), showing an increasing trend from the downstream to the upstream of the Dahuang River. The difference in the annual average tidal

* Corresponding author. Physical Oceanography Laboratory/CIMST, Ocean University of China and Qingdao National Laboratory for Marine Science and Technology, Qingdao, Shandong, 266100, PR China.
E-mail address: wsjang@ouc.edu.cn (W. Jiang).

https://doi.org/10.1016/j.ecss.2018.09.019
Received 29 January 2018; Received in revised form 14 August 2018; Accepted 19 September 2018
Available online 21 September 2018
0272-7714/

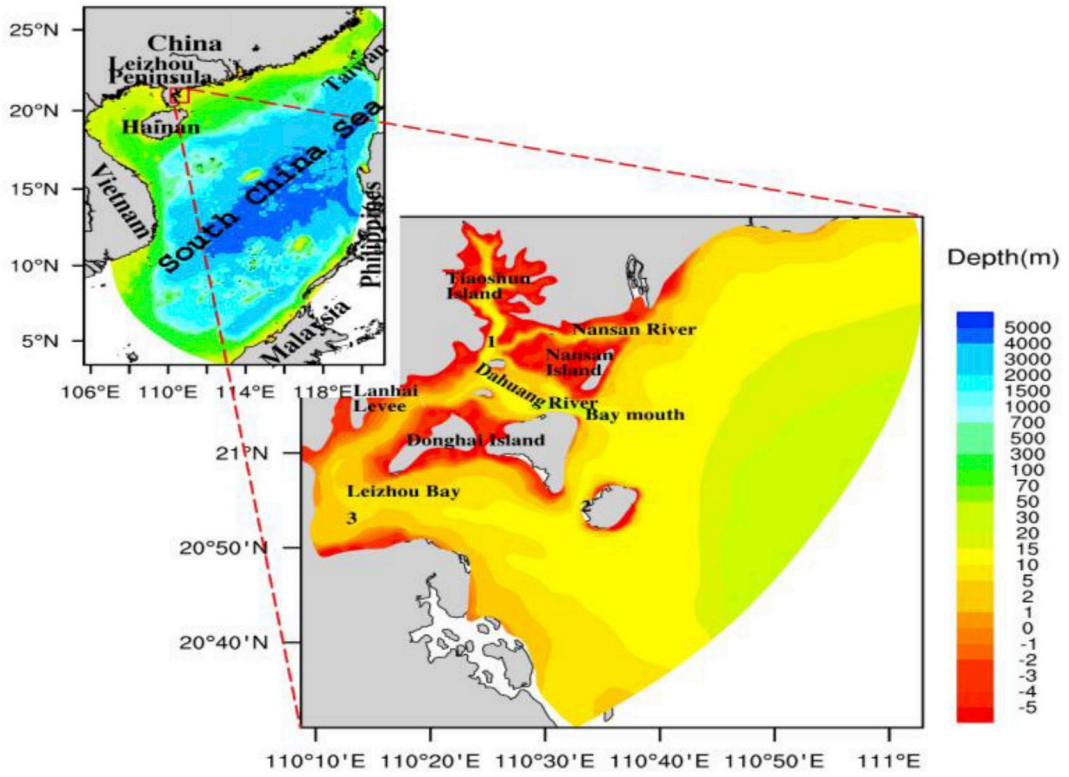

Fig. 1. The bathymetry of the model area. Locations 1, 2, and 3 are Zhanjiang, Naozhou, and Nandu tidal stations, respectively. The upper left and the lower right panels are the full domain and the subdomain of the model.

range between Tiaoshun Island in the upstream and the bay mouth is about 0.6 m and the annual maximum tidal range difference is 0.8 m (Ying and Wang, 1996).

The obvious tide distribution difference in the upper and lower reaches of ZH suggests that the storm surge may also have obvious local characteristics. In open sea waters, the distribution of the storm surge height is normally rather smooth over a relatively large area, hence many have studied the spatial distribution of storm surge events with coarse spatial resolution meshes (Flather, 1994; Flather and Smith, 1998; Lowe et al., 2001; Horsburgh and Wilson, 2007; Olbert and Hartnett, 2010; Haigh et al., 2014; Pasquali et al., 2015). However, in some nearshore areas and estuaries, the distribution of the storm surge may reveal an obvious regional feature only at a small spatial scale, and the coarse spatial resolution in many studies may preclude the capturing of regional features (Flather, 1994; Flather and Smith, 1998; Lowe et al., 2001; Haigh et al., 2014). Some researchers include small-scale features such as those in Guo et al. (2009), Jones and Davies (2009), and Dietrich et al. (2010), but they are confined to one or a small number of cases, which are insufficient to study the possible spatial distributions of storm surge in an area thoroughly.

Generally, the storm surge in a bay or an estuary can be regarded as the coupling of the local storm surge and non-local storm surge. The local storm surge is generated by local atmospheric forcing including the local winds and air pressure gradient at the sea surface in the study area. The non-local storm surge is the storm surge wave propagating from the sea area outside of the bay or the estuary being studied. The atmospheric forcing in the outer area is called the remote atmospheric forcing. In some places, there is a huge difference in the surge height between the upstream region and the downstream region due to the propagation of the non-local storm surge through a shallow and convergent estuary. Guo et al. (2009) study this phenomenon in the Hangzhou Bay of China, and their results show that in extreme cases, the surge height in the upper reach of the Hangzhou Bay can be twice that in the lower reach, which is mainly due to the shallowness and the narrowness of the upper reach of the Hangzhou Bay. Jones and Davies (2009) note that local atmospheric forcing has little effect on storm surge in the Mersey River, and the uneven distribution of storm surge within it is mainly due to the propagation of non-local storm surge through the gradually narrowing river. Soontiens et al. (2016) presents an example in a wider and deeper bay showing that storm surge height is also dominated by the remote atmospheric forcing-induced non-local surge.

However, in some other places, such as the Eastern Irish Sea, local and remote atmospheric forcing are of equal importance to the spatial distribution (Jones and Davies, 1998, 2009). Although Olbert and Hartnett (2010) point out that local atmospheric forcing is not that important in that particular area, they find that it still could account for 36% of the total surge in their study. The water surface slope generated by the local atmospheric forcing is also shown to be steep between lakes Pontchartrain and Borgne during hurricane Katrina (Dietrich et al., 2010).

Nevertheless, the contribution of local atmospheric forcing varies with wind direction, as shown by Shen and Gong (2009), by using prescribed steady wind fields. That is to say, the result obtained by considering only several sporadic storm surge cases is not comprehensive. In addition, sea level rise can affect the spatial distribution of the surge residual to a certain extent (Horsburgh and Wilson, 2007; Feng et al., 2014). Numerous studies have been performed for a future change in the sea level in 100 years (Chen, 1997; Soloman et al., 2007; Rahmstorf, 2007; Vemeer and Rahmstorf, 2009; Katsman et al., 2011) with the estimated average sea level rise ranging from 0.22 m to 1.90 m. In this paper, we make use of the sea level rise predictions proposed by the Soloman et al. (2007), with a lower one of 0.22 m and a higher one of 0.88 m, to find out how sea level rise affects storm surge in ZH. Among other factors, coastline change could also affect storm surge distribution (Zhang et al., 2013; Haigh et al., 2014).

In the present study, the spatial distribution of storm surge in a small-scale bay, ZH, is examined by establishing a high-resolution

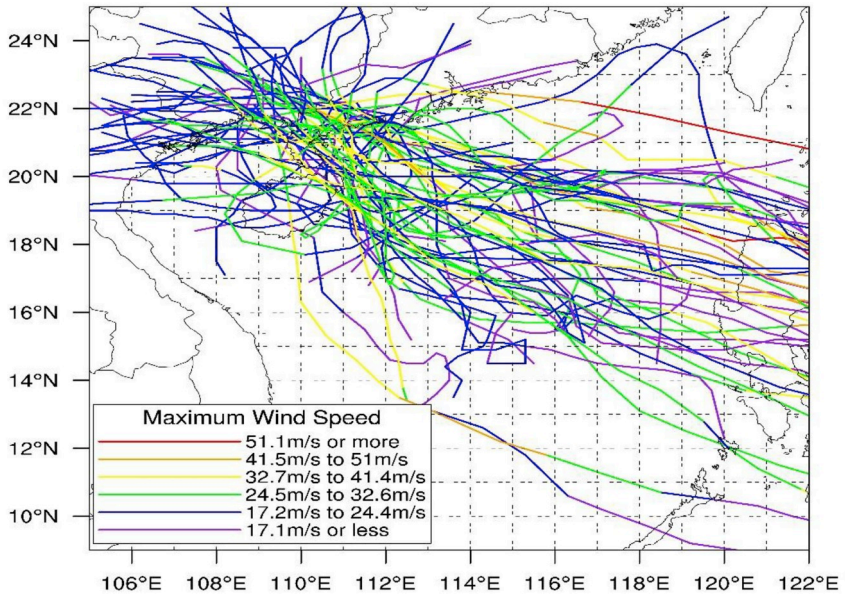

Fig. 2. The tracks and maximum wind speed of the 66 typhoons chosen in this study.

Table 1
Observation and simulation of the maximum storm surge residual of 10 historical tropical cyclones.

Stations		Typhoon IDs									
		6311	6508	7220	7406	8007	9615	9803	0307	0606	1117
Simulated Surge Residual (cm)	Naozhou							61	100	75	304
	Nandu					568			102		
	Zhanjiang	253	333	237	218	453	202		138		336
Observed Surge Residual (cm)	Naozhou							41	135	112	270
	Nandu					594			128		
	Zhanjiang	266	240	215	242	465	150		127		287
Relative Error (%)	Naozhou							49	−26	−33	13
	Nandu					−4			−20		
	Zhanjiang	−5	39	10	−10	−3	35		9		17

numerical model forced by historical storm surge events influencing that area in last 65 years. From the model results, the relative importance of local and remote atmospheric forcing on spatial distributions is estimated so that the mechanisms that produce them can be exposed. The effects of sea level rise and coastline changes on storm surge in that small-scale bay are presented as well.

The structure of the paper is as follows. Section 2 describes the model set up and data used in the study. Section 3 discusses various aspects of model validation. Section 4, the main part of our study, includes the following. Section 4.1 shows the regional features of storm surge in ZH and reveals how local and remote atmospheric forcing influence the spatial distribution of storm surge. Section 4.2 discusses the response of the surge distribution due to local and remote atmospheric forcing considering coastline change and sea level rise. The conclusion is given in Section 5.

2. Model set up and data

2.1. The storm surge model

The Advanced Circulation (ADCIRC) Model (Luettich and Westerink, 2004) is used to simulate historical storm surge events in ZH. The 2D barotropic model with a hybrid nonlinear bottom friction coefficient scheme is adopted, with the friction coefficient calculated by:

$$F = F_{min} \times \left[1 + \left(\frac{H_b}{H}\right)^{\theta}\right]^{\frac{\gamma}{\theta}}, \quad (1)$$

where F is the bottom friction coefficient; F_{min} is the minimum bottom friction coefficient (0.0025 in this study); H is the water depth; H_b is the threshold, beyond which the bottom friction transits from a Manning-type friction to a quadratic friction type; γ (0.3333 in the study) and θ (10 in the study) are dimensionless parameters utilized in the hybrid bottom friction scheme. To allow for the inundation of coastal areas, the wetting and drying scheme of ADCIRC is enabled.

A nesting technique is used in this study to distinguish the local atmospheric forcing from the remote atmospheric forcing. By setting an open boundary for the subdomain, we were able to force the subdomain either with or without remote atmospheric forcing. This can also balance the demands of high resolution in ZH and the associated computation costs. As shown in Fig. 1, the full domain covers most of the South China Sea, and the subdomain only occupies a small area surrounding ZH. There are 36367 elements and 18606 nodes in the full domain with the resolution varying from 0.7 to 20 km. In the subdomain, there are 27487 elements and 14607 nodes with the resolution varying from 0.18 to 3 km. The time step used in the model is 3 s.

The full domain is driven by atmospheric forcing at the surface and surge elevation inversed from the sea surface atmospheric pressure at the open boundary. The boundary condition to force the surge in the subdomain is the time series of the water level on each boundary nodes, which includes both the tide elevation of 8 major constituents (M2, S2,

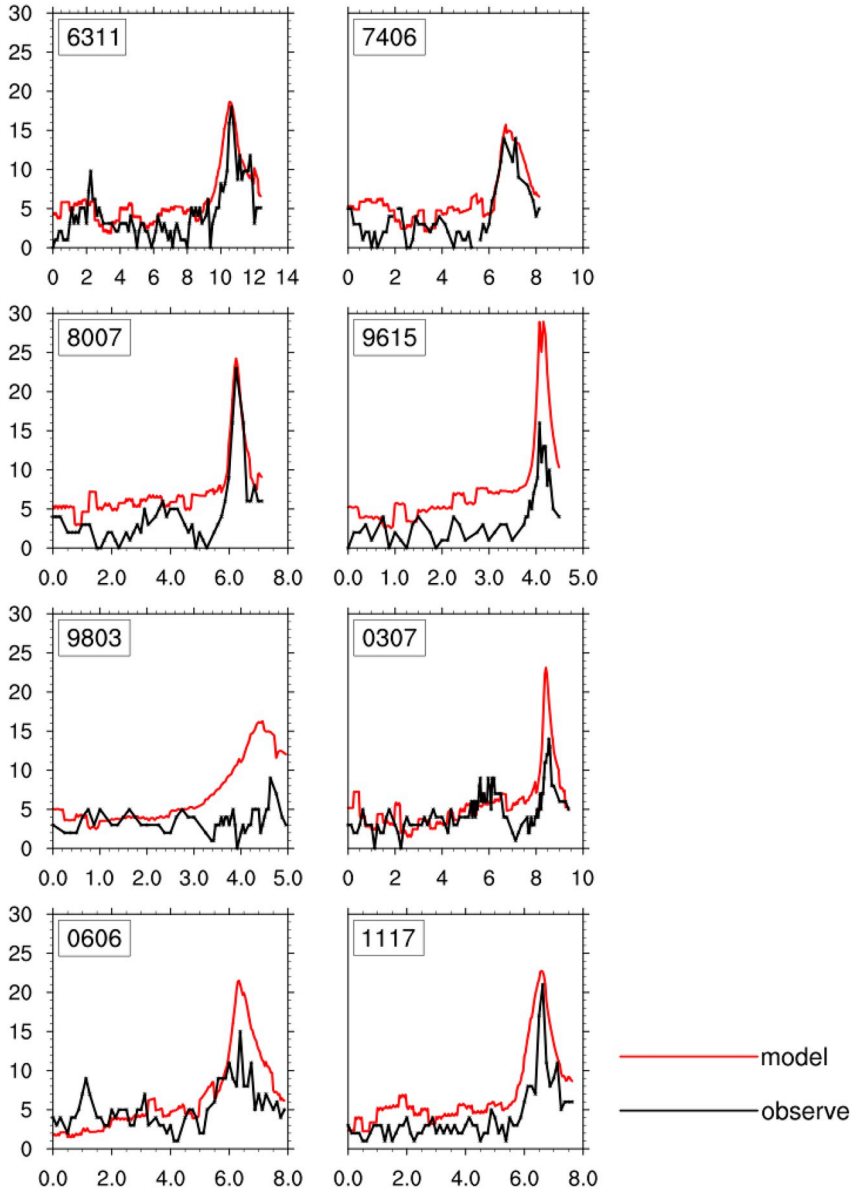

Fig. 3. Wind speed (m/s) versus time (day) in 8 events at Zhanjiang station.

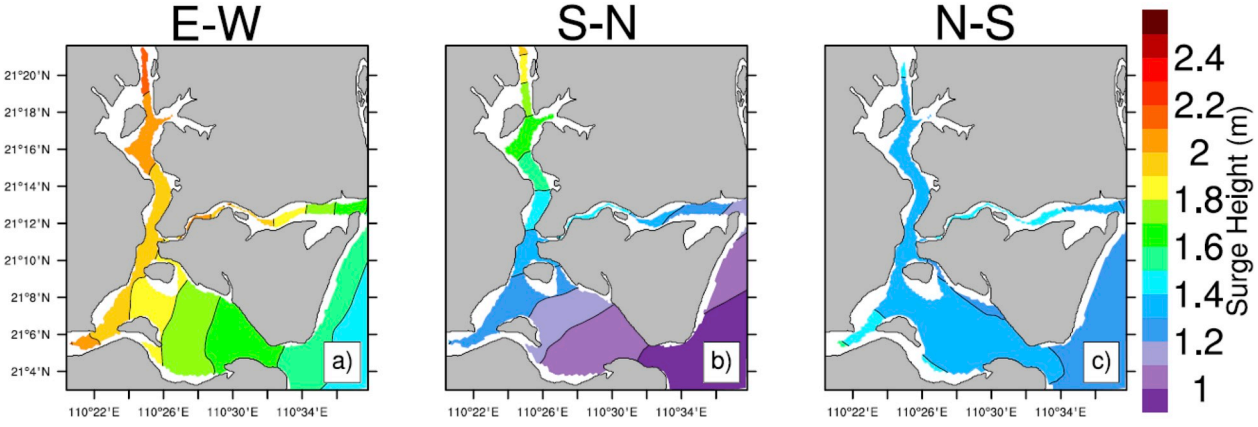

Fig. 4. The averaged surge height of the a) E-W, b) S-N, and c) N-S cases.

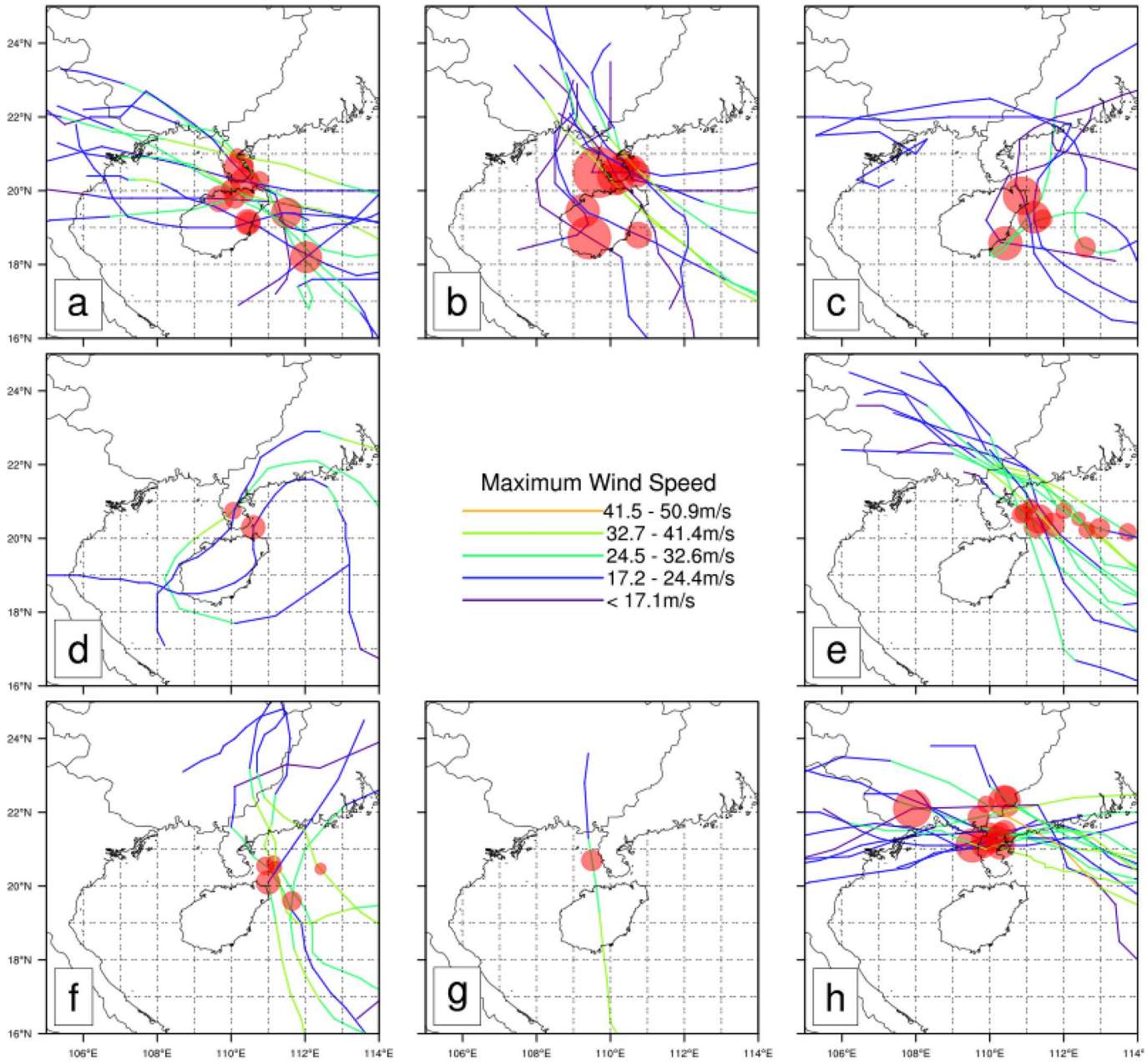

Fig. 5. The typhoon track sets associated with the E-W, S-N, and N-S patterns. The centers of the red disks denote the locations of the typhoon centers at the time of occurrence of the maximum surge (TMS), and the radius represents the radius of maximum winds. Pictures a-h correspond to Class A-H. (For interpretation of the references to colour in this figure legend, the reader is referred to the Web version of this article.)

N2, K2, K1, O1, P1, and Q1) in that area from OSU Tidal Prediction Software (Egbert and Erofeeva, 2002) and the surge elevation extracted from the full domain results. A tide model is also run in the subdomain with only the tidal signal including the same 8 constituents being applied at the open boundary. Therefore, the surge elevation for the subdomain is obtained by deducting the tidal elevation from the total elevation. This method is a traditional nesting technique. It loses some accuracy due to the lack of wetting and drying status on the land boundaries (Baugh et al., 2015). However, most of our land boundaries have a relatively high elevation and are out of the reach of storm surge. Hence, the effect of wetting and drying on the boundary should be within a reasonable range. A new subdomain modeling method developed by Baugh et al. (2015), which provides not only the water level but also the velocity and the dry-wet condition, can be utilized in the future to see whether other conditions affect the results.

To quantify the influence of local and remote atmospheric forcing on surge height, the remote atmospheric effect (RAE) is defined as the maximum surge at each node raised only by remote atmospheric forcing, which is the water level on the open boundary of the subdomain; the local atmospheric effect (LAE) is defined as the difference between the total maximum surge height and RAE; and the local atmospheric contribution (LAC) is the contribution of LAE to the total surge height, which is defined as LAE divided by the total maximum surge height at each node.

2.2. The wind model

In this study, the atmospheric forcing field is calculated based on the empirical typhoon formula. The circular storm wind velocity is described by the formula of Jelesnianski (1965),

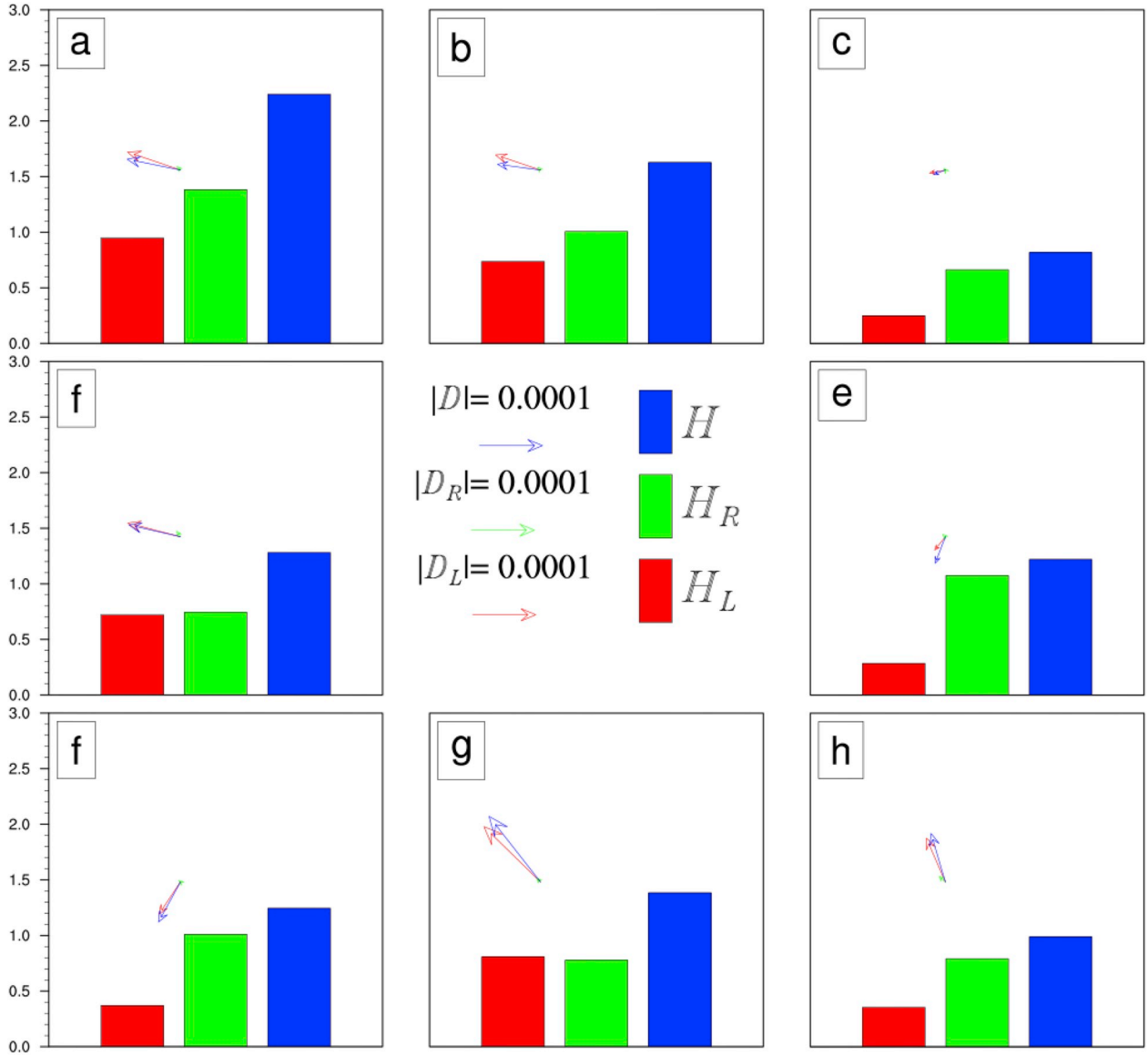

Fig. 6. The local, remote, and entire meteorological field induced averaged surge height (in meters, represented by H_L, H_R, and H) and surge orientation vector of LAE, RAE, and total surge height (represented by $\boldsymbol{D_L}$, $\boldsymbol{D_R}$, and $\boldsymbol{D}$). Pictures a-h correspond to Class A-H.

$$V_r = V_{max}\frac{2^{\frac{r}{r_{max}}}}{1+\left(\frac{r}{r_{max}}\right)^2}, \tag{2}$$

where r is the distance to the center of the typhoon; V_{max} is the maximum wind speed; r_{max} is the radius of maximum wind.

The additional wind velocity V_d induced by the moving of the typhoon center is also added to the wind speed according to Jelesnianski (1965). V_c is the movement speed of the typhoon center.

$$\boldsymbol{V_d} = \begin{cases} \boldsymbol{V_c}\frac{r}{r+r_{max}} & 0 \le r \le r_{max} \\ \boldsymbol{V_c}\frac{r_{max}}{r+r_{max}} & r_{max} \le r < \infty \end{cases} \tag{3}$$

The surface wind is defined as,

$$\boldsymbol{V} = \boldsymbol{V_d} + \boldsymbol{V_r}$$

The pressure field is derived according to the geostrophic wind relation (Guan et al., 2000),

$$P = P_\infty - \frac{P_\infty - P_c}{1+\left(\frac{r}{r_{max}}\right)^2}. \tag{4}$$

Unfortunately, r_{max} and V_{max} in the above equations are not included in the data; they are estimated empirically as follows.

r_{max} is approximated by fitting a curve of the tropical cyclone radius, as proposed by Jiang et al. (2008):

$$r_{max} = 1119\,(P_\infty - P_c)^{-0.805}. \tag{5}$$

V_{max} is estimated by the wind-pressure relationship proposed by Atkinson and Holliday (1977):

$$V_{max} = 3.0\,(P_\infty - P_c)^{0.644}, \tag{6}$$

where P_∞ is the ambient pressure taken as 1010 hPa; P_c is the central surface pressure obtained from the typhoon best track dataset.

It should be noted that the first parameter on the right side of Eq. (6) is 6.7 in the original formula in Atkinson and Holliday (1977), but the unit of the wind speed is knots there, and it is used to calculate the 1-min-averaged maximum sustained surface wind speed; the wind speed unit used in this study is m/s, and the 10-min averaged wind is recommended for use in ADCIRC. According to Atkinson (1974), the 10-min averaged maximum wind speed can be obtained by multiplying 0.88 to the 1-min averaged maximum wind speed. Thus, the parameter

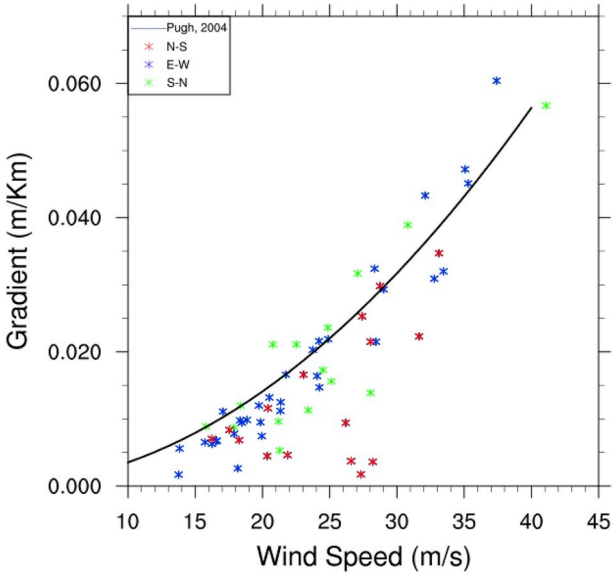

Fig. 7. Maximum surge gradient versus the maximum wind speed at Zhanjiang Station, each mark represents a storm surge process.

Table 2
The scenarios of the experiment (△p ranges from −10 to 10 by 5).

	central surface pressure	radius of the maximum wind	maximum wind speed
Group1	p + △p	r_max (p)	h_max (p)
Group2	p	r_max (p + △p)	h_max (p)
Group3	p	r_max (p)	h_max (p + △p)
Group4	p + △p	r_max (p + △p)	h_max (p + △p)

of 3.0 is obtained after this transformation.

2.3. The topography data and the typhoon data

In the full-domain, the ETOPO1 1-Minute Gridded Global Relief Data Collection (Amante and Eakins, 2009) is used as the water depth data. In the subdomain, the depth data comes from the sea chart published by China Navy Hydrographic Office. To take the floodplain into consideration, the Shuttle Radar Topography Mission (SRTM) data (Jarvis et al., 2008) with a resolution of 3 ″ is used as the altitude data. The 1985 National Elevation Reference commonly used in China is 35.7 cm higher than the EGM96 geoid used by the SRTM data (Guo et al., 2004), therefore, the data in our model is obtained by subtracting 35.7 cm from the original data. Since the resolution of the digital elevation data is about 100 m, the finest mesh resolution used in this study is of the same magnitude.

The typhoon data comes from the best track dataset of tropical cyclones from China Meteorological Administration (tcdata.typhoon.gov.cn) (Ying et al., 2014). The dataset records typhoons occurring between 1949 and 2013, and from those we select ones with landing points that are within 200 km of the central point of the coastline of ZH (Li et al., 2016).

3. Model validation

Since storms with only mild impacts give rise to an irregular distribution of the surge residual. Thus, only those with a simulated surge residual in excess of 0.5 m at Zhanjiang tide gauge Station (Fig. 1) are considered in this study. Therefore, a total of 66 storm surge events between 1949 and 2013 are included (Fig. 2). To validate the model simulation results, the simulated maximum surge height was compared with the observed value during 10 typhoon processes. The observation results during those events are taken from Chen et al. (2002), Ma and Hu (2004), Wang et al. (2008), Zhang et al. (2009), Shi and Huang (2013) and the State Oceanic Administration of China. The verification results are shown in Table 1.

The results show that in most of the cases the maximum surge residual simulated by the model is close to the observed values, but in some other cases, the model results are unreasonable and may be related to the empirical model we used. In the typhoon diagnostic model, the radius of maximum wind is completely taken as a function of the central surface pressure. This is because in actual cases the statistical results show that the radius of maximum wind decreases with decreasing central surface pressure. But in practice there may be a large deviation, say, as in Katrina, which had extremely low central surface pressure as well as a large radius of maximum wind, led to a serious disaster (Fritz et al., 2007; Irish et al., 2008). The effect of wind wave is also ignored (Jelesnianski, 1965), which neglects the asymmetric wind field pattern affected by asymmetric wave fields. Furthermore, it omits the bottom friction of typhoons (Jelesnianski, 1965), which may lead to higher wind speed than it actually is when making landfall. Thus, our study may overestimate the effect of the wind stress. The modeled and observed wind speed comparison at Zhanjiang Station is shown in Fig. 3. The observation dataset comes from National Centers for Environmental Information (website: https://www.ncei.noaa.gov/) and has a 3-h temporal resolution. Typhoons 9803, 9615, 0307, and 0606 have much stronger model wind than observed wind, which leads to large surge errors compared to historical records.

4. Results and analysis

4.1. The spatial distribution patterns of the maximum surge

In order to study the spatial distribution of the storm surge residual within the bay, the maximum storm surge height of each wet grid point within the bay during each typhoon process was recorded for investigation. Ahead of the discussion on how different variables affect the distribution pattern, we first have to categorize the distributions. For disaster prevention, the maximum surge elevation is of great concern, although the maximum elevation of a storm surge does not appear simultaneously at different locations for every case. So in this study the maximum surge elevation is used as an index.

4.1.1. The way to distinguish the spatial distribution patterns

The distribution pattern of the maximum surge varies from case to case; we can define the surge orientation vector $\boldsymbol{D}$ to express the orientation of the water increase in ZH.

$$\boldsymbol{D} = \left(\sum_{i=1}^{n} S_i \boldsymbol{D}_i \right) / \sum_{i=1}^{n} S_i \tag{7}$$

where $\boldsymbol{D}_i$ is the vector of the maximum surge level gradient on x-y plane of every grid element in ZH; S_i is the area of each element of the mesh. Then α, the orientation of the vector $\boldsymbol{D}$ relative to the east direction in the Cartesian system, can be easily obtained. According to the value of α we define the water distribution pattern with $315° > \alpha \geq 225°$ as the N-S pattern, $135° > \alpha \geq 45°$ as the S-N pattern, and $225° > \alpha \geq 135°$ as the E-W pattern.

Of all the 66 cases, 17 have an N-S pattern, and 16 have an S-N pattern, and 33 have an E-W pattern. The averaged distribution of the cases in different categories of each node is shown in Fig. 4. The maximum surge height in the E-W category grows from east to west; the one in the S-N category grows from southeast to northwest, and the one in the N-S category grows from northeast to southwest. Since the surge elevation is caused by both the local and remote atmospheric forcing, LAE and RAE are presented for each of the three categories of the typhoon storm surge in ZH in the following.

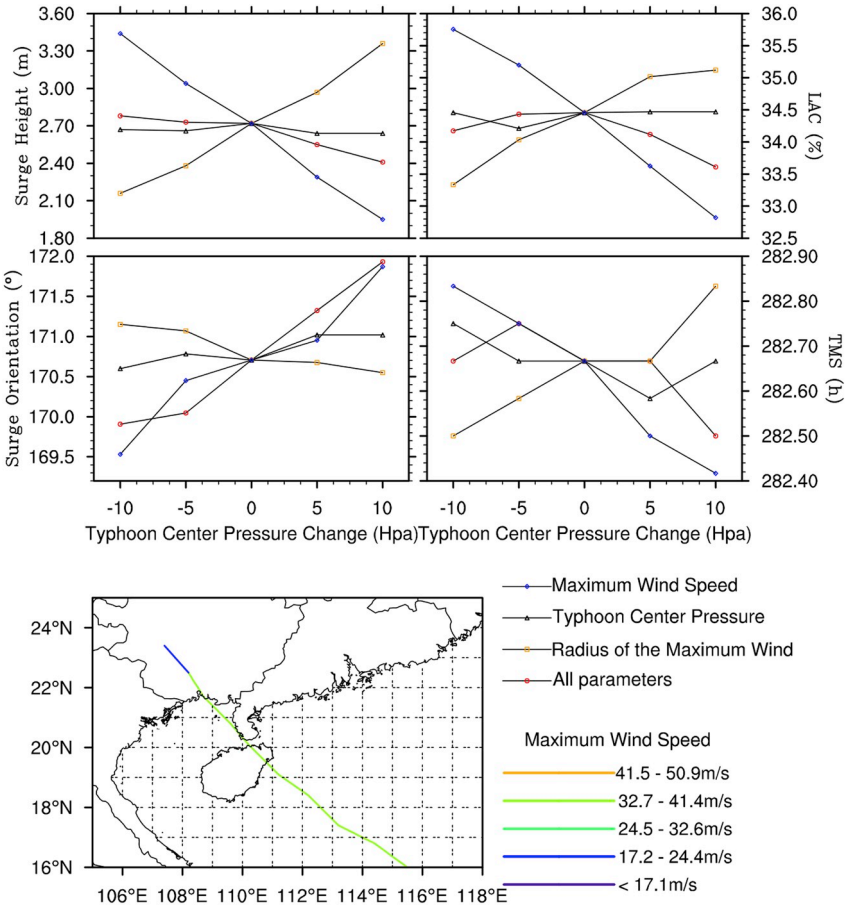

Fig. 8. The maximum surge residual, LAC, surge orientation, and TMS of Zhanjiang Station in the 4 groups of the experiments.

4.1.2. The influence of the typhoon track on the spatial distribution pattern

When analyzing the distribution patterns, we find that the formation of the patterns can be clearly explained by the typhoon track and in some cases the intensity as well. The typhoon tracks in each pattern have their own features: only a few tracks of N-S and E-W category and S-N and E-W category are alike because the E-W pattern is a transitional pattern between the N-S and S-N patterns. To reveal how the typhoon track influences the distribution pattern, we introduce the time of occurrence of the maximum surge (TMS) at Zhanjiang Station. The typhoon tracks leading to same surge pattern are drawn in one subfigure and the location of the typhoon center at TMS is also denoted by a red disk on the typhoon track in Fig. 5.

In Fig. 5, for the storms leading to the E-W pattern, 4 classes can be further categorized according to their tracks and intensity. The storms of class A hit the southeastern coast of Leizhou Peninsula and Hainan Island in the area of 18–21°N, 110–112°E, then continue to the west; typhoons of class B are similar to class A in the first half, while they turn north after passing 110°N; typhoons in class C hit the same area as well as the first 2 classes at first, but they turn north before crossing 110 N; typhoons of class D, which are completely different from the first 3 classes, come from the northeast of ZH and travel southeastward.

The storms leading to the N-S category are divided into classes E and F. The typhoons in class E first travel to the southeast waters in 20–21°N, 111–114°E, then continue northwestward and cross the center and the north of the ZH; the storm tracks in class F are like those in class C, while the intensity of the storms is not – the intensity of the ones in class C is smaller than those in class F. According to Eqs. (5) and (6), higher pressure shrinks the local winds in ZH and amplify the radius of the largest wind speed, which may lead to an earlier TMS. The typhoon tracks of the S-N category are relatively straightforward – one is from the south to the north across the west of ZH (class G), and the other is from the east to the west across the north of ZH (class H).

It is obvious that the locations of typhoon centers at the TMS in each class are considerably aggregated. The typhoon centers at TMS of E-W category are around the southern and eastern coast of Leizhou Peninsula and Hainan Island at 109–111°E, 18–21°N (Fig. 5a and b, c, and d). For the N-S category, the typhoon centers are almost on the ocean area of 111–114°E, 20–21°N (Fig. 5e and f). For the S-N ones, the centers are mostly on the west and northwest of ZH around 119-111°E, 21–23°N (Fig. 5 h).

Coincidently, the TMSs are very close to the occurrence time of the maximum surge height induced only by the subdomain boundary water elevation (denoted as TMSR later) with the difference between them being 2.3 h. The occurrence time of the maximum surge height driven only by LAE is denoted as TMSL, which derived by finding out the time of the maximum difference between the total maximum surge height and RAE induced maximum surge height. The difference between TMS and TMSL is about 15.3 h. It indicates that the tracks influence the locations of the centers at TMS mainly through RAE.

To make clear whether it is RAE or LAE that has a larger effect on the distribution and the surge height, the surge orientation vector and the mean elevation of LAE, RAE, and total surge are plotted in Fig. 6. The averaged surge in Fig. 6 is calculated by

$$H = \frac{\sum_{i=1}^{n1} S_i E_i}{\sum_{i=1}^{n1} S_i} \tag{8}$$

where H is the averaged surge height for ZH, E_i is the averaged surge height for the three vertices of an element. H_R is the averaged surge height for the result of the subdomain without local wind, and H_L is the difference between H and H_R. Also, $\boldsymbol{D_L}$ is the difference between $\boldsymbol{D}$ and

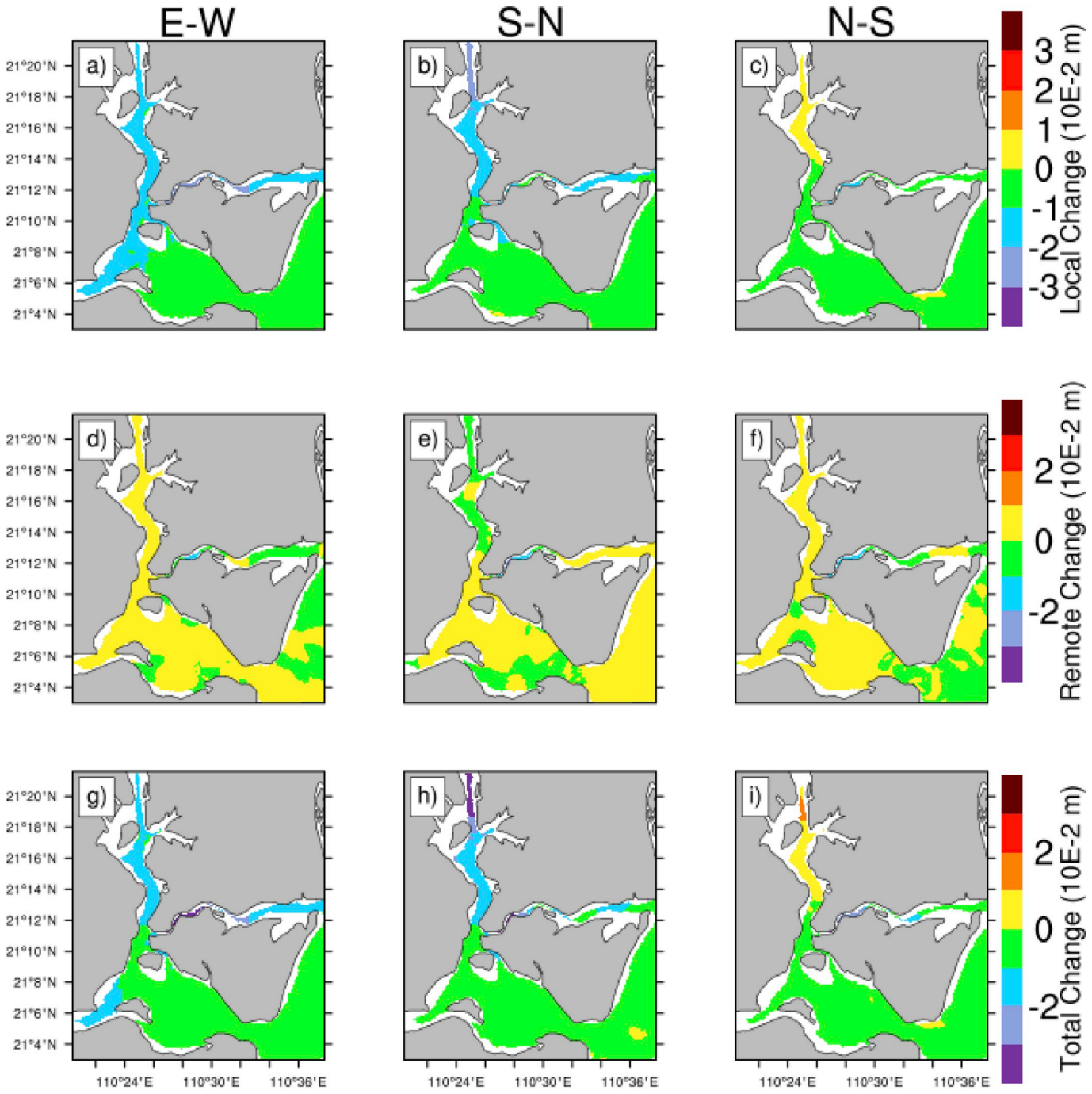

Fig. 9. The change of the surge because of the 0.22m sea level rise.

$\boldsymbol{D_R}$ where $\boldsymbol{D_R}$is the surge orientation vector $\boldsymbol{D}$ of RAE calculated by Eq. (7).

As is shown in Fig. 6, $\boldsymbol{D_L}$, $\boldsymbol{D_R}$, H_L, and H_R vary with different classes. However, $\boldsymbol{D}$ is highly consistent with $\boldsymbol{D_L}$, while $\boldsymbol{D_R}$ is not. RAE is not relevant to the spatial distribution in most cases. In classes A, B, E, F, and H, H_L is less than H_R, particularly in classes C, E, F, and H. RAE is ahead of LAE in the contribution to the surge height in most classes, but LAE cannot be ignored. Thus, it is reasonable to conclude that the distribution is dominated by local winds when the outer area water elevation reaches its peaks (or a little later, considering it takes some time for the water travel from the boundary to inner areas). In addition, typhoons that come from the east to the west and cross the south of ZH are the most dangerous ones (Fig. 6 a).

The reason LAE controls the distribution pattern in ZH can be explained as follows. Compared with the Strait of Georgia in Soontiens et al. (2016), ZH is a shallow bay area and forced by relatively much stronger winds of typhoon other than extratropical storms. According to Pugh (2004), the steady state sea level gradient can be calculated by:

$$\text{slope} = \frac{C\rho_{air}U^2}{g\rho Dc}, \tag{11}$$

where C is the coefficient of friction; ρ_{air} is the air density; U is the wind speed; g is the gravitational acceleration; ρ is the density of water; Dc is the depth of the water. We can take the average surge heights of the left bottom of ZH and the mouth of it in E-W cases as an example. The distance between them is about 16 km; the Dc is about 8.1 m as the average depth; suppose U is 25 m/s which is somewhat close to the average maximum speed of the winds affecting ZH; C is equal to

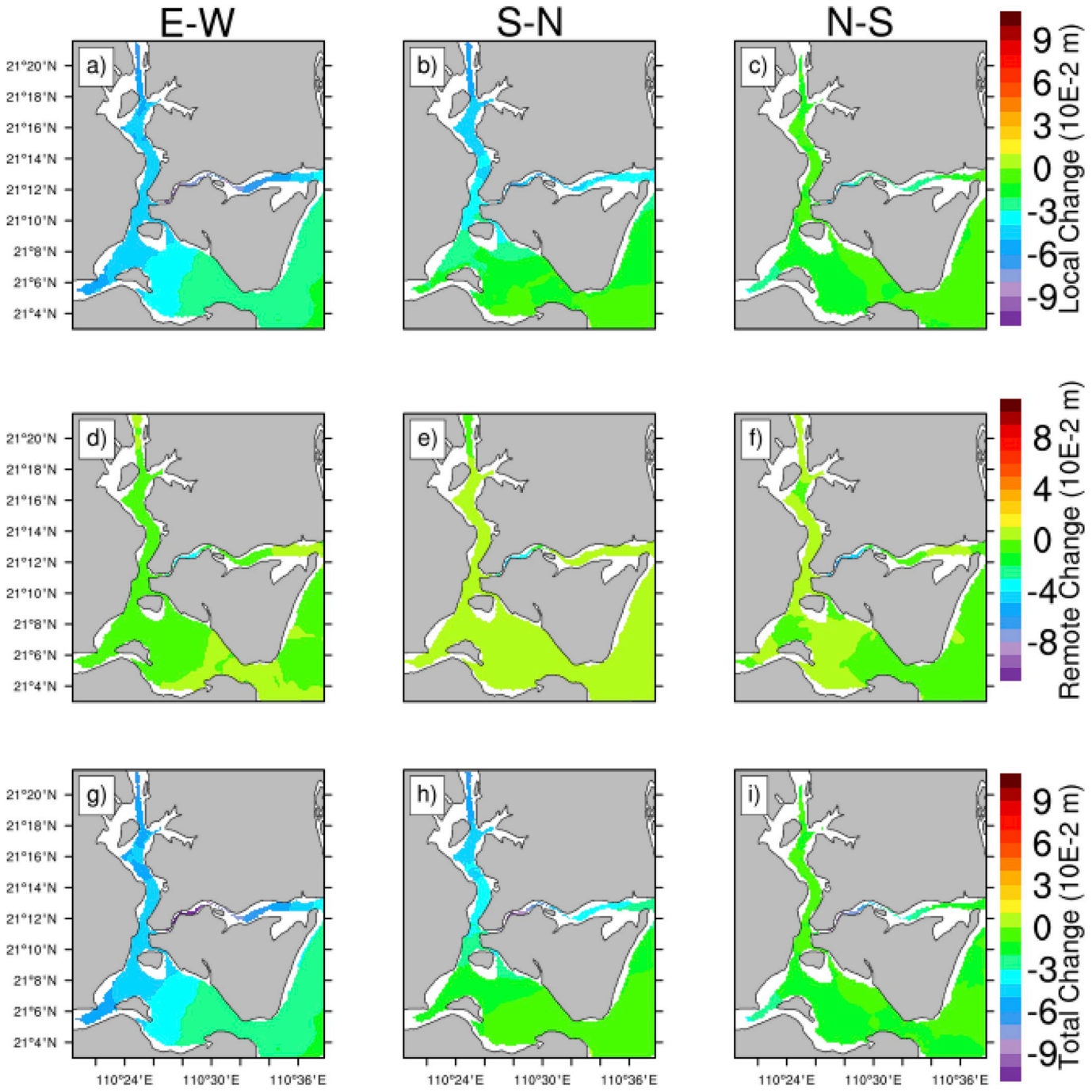

Fig. 10. The change of the surge because of the 0.88m sea level rise.

0.0025, where depth is more than 1m, ρ and ρ_{air} are 1028 kg/m^3 and 1.15 kg/m^3, respectively; and g is 9.80 m/s^2. We can obtain the gradient, which is about 2.22 – 10^{-5}, and the water level difference between them is 0.34 m, which is close to the simulation results. This shows that in shallow waters, under the condition of strong winds, LAE will soon reach a steady state: storm surge comes fast and fierce, and adjacent areas can also be prone to different disaster situations. The shape of the bay also helps to form this outcome. Compared to the Mersey River mentioned in the paper of Jones and Davies (2009), ZH has a wider river width at the downstream which make it possible to have a distinct cross-river distribution difference divergence, and the lambdoid shape provides a possibility for the water to cumulate in various directions to form the patterns. We plot the maximum surge gradient versus the maximum wind speed for each case in Fig. 7. It shows that in most of the S-N and E-W cases the surge gradients are close to the estimated value of Pugh (2004). While in N-S cases, a third of the gradients are remarkable below the estimated value. One possible situation that accounts for this is that in many N-S cases, the maximum surge height on each area occurs at different moments, which means in these cases it is difficult for the surge to reach a steady state; the other possible situation is that the maximum surge height occurs when the wind is not at its peak. For instance, in category H, the typhoon centers at TMSs aggregate at the west of ZH after passing ZH, and the wind speeds decrease at ZH because of the negative migration wind velocity. The other phenomenon we notice in Fig. 7 is that the gradient below the estimated value is more likely to appear at lower maximum wind speed. It shows that when the wind is stronger, it is more likely to reach a steady state.

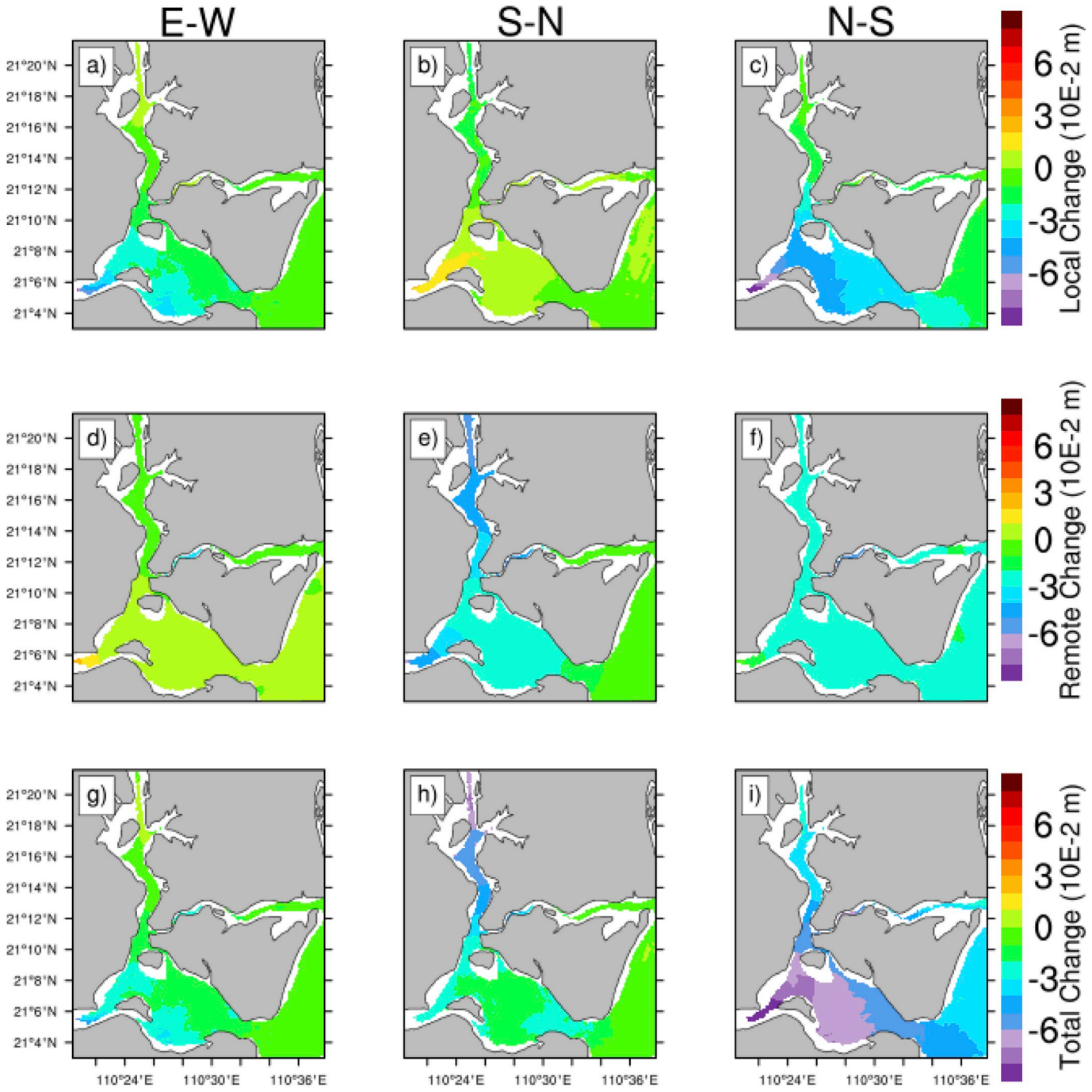

Fig. 11. The change of surge because of the removing of the Lanhai levee.

4.1.3. The influence of the intensity of the typhoon on the patterns

The intensity of a typhoon also influences the distribution pattern in ZH. In this study, the intensity of a typhoon is determined by several factors including central surface pressure, the maximum wind speed, and the radius of the maximum wind. Since the maximum wind speed and the radius of maximum wind in the present study are determined by the central surface pressure alone, through the use of formulas (3), (5), and (6), we describe a series of the experiments that assess the influence of typhoon intensity on the surge patterns by varying the central surface pressure in a typical typhoon surge in ZH. Typhoon 8411 (Typhoon IKE), an E-W category storm, is selected as a typical typhoon, which causes rather a strong storm surge with a relatively straight typhoon track and a smooth surge elevation curve.

The experimental setup is listed in Table 2, and there are 4 groups of experiments in this study. For groups 1, 2, and 3, only the central surface pressure, the radius of maximum wind, and the maximum wind speed is changed, while in group 4 all the three variables are changed together. In each of the 4 groups, $\triangle p$ is changed from -10 hPa to 10 hPa by every 5 hPa. Thus, there are 5 scenarios in each group and 17 scenarios (when $\triangle p$ is equal to 0, all the 4 groups are the same) are set to form 4 groups of the experiment, which are carried out in this study.

In each of the 17 scenarios, we take the maximum surge residual and its orientation as the index to estimate the influence of the three parameters on the distribution. LAC is considered to exhibit the weight change of LAE. TMS of each scenario is also chosen as another index. The results of the above 4 indexes for 17 different scenarios are shown in Fig. 8. In the first group, the increase of the central air pressure decreases the maximum surge height, while the LAC increases since the

local wind is left unchanged in the experiment. But both the maximum surge height and the LAC in ZH remain rather steady when only the central air pressure varies in the experiment. This shows that the intensity of the storm surge in such a shallow area as ZH is not controlled directly by the central air pressure alone because the inverted barometer term has a weak impact on the coastal area like ZH. The surge orientation as well as TMS slightly change in this group. The orientation is more southerly and TMS occurs a little earlier.

In the second group of the experiment, the radius of maximum wind increases with the rise of the central surface pressure according to Eq. (5). We can see that the positive change in the radius of maximum wind obviously enhances the surge height in ZH. LAC also increases sharply because the local high wind speed area amplifies along with the increase of the radius of maximum wind. Within the 5 experiments of this group, the surge orientation is more northerly and TMS is delayed when the radius of maximum wind is larger.

Since the maximum wind speed decreases with the rise of the central surface pressure according to Eq. (6), the surge residual has a decreasing trend with the increase of the central air pressure. It is also natural to find LAC decreasing because the maximum wind speed decreases. The surge orientation is more northerly when the maximum wind speed decreases. The effect of maximum wind speed seems to be stronger than the other 2 factors on the TMS – the stronger the wind is, the later the TMS comes.

Three factors are combined to form the fourth group of the experiments. Because the central air pressure alone only has little influence on the maximum surge height, the influence on the maximum surge residual is mainly from the two opposite effects of the variation of the radius of maximum wind and the maximum wind speed. It can be found that the two effects are almost linear in a certain range. But the maximum wind speed has a slightly stronger influence on the maximum surge residual, which is reflected by the fact that the surge residual is going down when the central surface pressure shows an upward trend.

From Fig. 8 we find that the LAC has a positive correlation with the maximum surge height, i.e., the stronger the storm is, the greater the LAC. This hints that during a severe storm surge the accurate local meteorological forecasting is greatly needed. The factors not only change the surge height and the share of LAE but also change the distribution pattern, although not much in this case. In this case, TMS comes earlier when the typhoon is weaker; the most important factor is the wind speed. When considering the influence on the surge orientation, the radius of the maximum wind and maximum wind speed are both important, but they play opposite roles.

4.2. The response of the maximum surge patterns to the sea level rise and the coastline change

4.2.1. The response to the sea level rise

All 66 cases of the typhoon storm surge are run twice with the 0.22 and 0.88 m sea level rise scenarios. It is found that the grouping of the typhoon cases according to the maximum distribution pattern does not change. But the distribution patterns of the maximum surge height change in the two future scenarios that are shown in Fig. 9 and Fig. 10. A general understanding is that LAE is weakened while RAE is strengthened because of sea level rise. In the cases of the E-W category, the change of LAE is somewhat stronger than that of RAE. This results in the reduction of the total surge residual in ZH. LAE change also exceeds RAE change in the S-N and N-S category. For all the categories LAE is stronger in the southwest corner and the east half part of the Nansan River, which is most likely because of the shallow water depth there. The magnitude of the maximum surge also increases. The value of the total surge height increase is of one order smaller than that of the sea level rise. That means the increase of the surge residual itself does not play the most important role in the aggravation of the storm surge disaster in ZH due to the sea level rise. But its effect on the tide amplitude and the sea level rise itself may lead to a considerable increase to the storm surge as pointed out in other studies (Feng et al., 2014).

4.2.2. The response to the change of coastline

In this section, the results of the cases with and without the barrier in the southwest corner of ZH are compared. The barrier blocks the water exchange between ZH and Leizhou Bay, and the surge residual as a result increases a little compared to the no-levee case. The distribution pattern changing trend in the EW and NS categories are almost the same, although the magnitude of the change is different. The surge increases about 8 cm on the east side of the levee compared to unclosed ZH in N-S and about 5 cm at the same area in E-W category; while the other areas are obviously increasing less than that on the east side of the levee. The change in the S-N category is completely different from the former two, where the maximum increase of surge residual occurs in the north, while the change around the levee is not obvious (see Fig. 11).

5. Conclusions

The impacts on the surge spatial distribution of LAE, RAE, and sea level rise, as well as shoreline changes, are discussed in this paper. In ZH, LAE and RAE both play important roles in the distribution of the surge residual. On average, RAE is dominant in the surge residual and TMS in most storm surge events, but it is not crucial to the spatial distribution. Due to distinct local features, LAE and RAE may play different roles in the storm surge distribution. In this particular area, a relatively broad bay width provides enough space for local winds to force water; the lambdoid shape makes it possible to gather water in different directions; the shallow water depth and strong winds bring about high water level gradient. The above characteristics make LAE more powerful in ZH than in the waters that are wide and deep (Soontiens et al., 2016) or shallow but narrow (Jones and Davies, 2009).

The quantitative method is able to categorize the distribution patterns, and the maximum surge residual distribution pattern can be divided into 3 categories. They are the E-W, N-S, and S-N patterns. In each pattern, the positions of typhoon centers at TMS are aggregated, and it is highly associated with RAE. The direction of the local winds at TMS gives rise to the maximum surge residual distribution pattern. The typhoon track is the dominant factor to maximum surge residual distribution pattern while the typhoon intensity plays the minor role, but the stronger the typhoon is, the more crucial LAE is. In strong storm surge events, the local effect is even more significant. This reminds us that, for disaster prevention and mitigation, plans must be drawn up according to specific typhoon tracks, and vulnerable areas must be strengthened to avoid major losses. In storm surge events, both maximum wind speed and radius of maximum wind are vital, but to some extent, the maximum wind speed is a little more important than the radius of the maximum wind.

At the same time, the present study sets up two sea level rise scenarios. Our conclusions show that in the case of sea level rise, the trends of the changes for LAE and RAE are opposite, though the magnitudes are basically equal. In general, E-W category storm surges are weakened, and the changes of N-S and S-N category storm surges are non-uniform and their patterns are inverted; there is a trend of reducing water gradient in all these cases. However, because the change of the surge residual is far less than the change of sea level, the most important consideration should be the sea level rise itself rather than its impact on the surge residual, as suggested by Feng et al. (2014). The surge residual within the bay increases due to the establishment of the sea embankment.

Acknowledgements

We gratefully acknowledge the support from the funding from National Key R&D Program of China (Grant No. 2016YFC1401504),

Public Science and Technology Research Funds Projects of Ocean (201305020-4), and China Scholarship Council (No. 201606330011).

Appendix A. Supplementary data

Supplementary data to this article can be found online at https://doi.org/10.1016/j.ecss.2018.09.019.

References

Amante, C., Eakins, B.W., 2009. ETOPO1 1 Arc-minute Global Relief Model: Procedures, Data Sources and Analysis. US Department of Commerce, National Oceanic and Atmospheric Administration, National Environmental Satellite, Data, and Information Service, National Geophysical Data Center, Marine Geology and Geophysics Division, Colorado, pp. 19.

Atkinson, G.D., 1974. Investigation of Gust Factors in Tropical Cyclones (No. FLEWEACEN/JTWC-TN-74-1). Fleet Weather Central/Joint Typhoon Warning Center Apo San Francisco 96630.

Atkinson, G.D., Holliday, C.R., 1977. Tropical cyclone minimum sea level pressure/maximum sustained wind relationship for the western North Pacific. Mon. Weather Rev. 105 (4), 421–427.

Baugh, J., Altuntas, A., Dyer, T., Simon, J., 2015. An exact reanalysis technique for storm surge and tides in a geographic region of interest. Coast Eng. 97, 60–77.

Chen, J., 1997. The impact of sea level rise on China's coastal areas and its disaster hazard evaluation. J. Coast Res. 925–930.

Chen, Y., Dong, Z., Jiang, G., 2002. Characteristic analysis of Zhanjiang Harbor's storm surge. Mar. Forecasts 19 (3), 44–52 (In Chinese).

Dietrich, J.C., Bunya, S., Westerink, J.J., Ebersole, B.A., Smith, J.M., Atkinson, J.H., Cardone, V.J., 2010. A high-resolution coupled riverine flow, tide, wind, wind wave, and storm surge model for southern Louisiana and Mississippi. Part II: synoptic description and analysis of Hurricanes Katrina and Rita. Mon. Weather Rev. 138 (2), 378–404.

Ding, W., 1986. Distribution of tides and tidal currents in the South China Sea. Oceanol. Limnol. Sinica 17 (6), 468–480 (In Chinese).

Egbert, G.D., Erofeeva, S.Y., 2002. Efficient inverse modeling of barotropic ocean tides. J. Atmos. Ocean. Technol. 19 (2), 183–204.

Feng, J., Jiang, W., Bian, C., 2014. Numerical prediction of storm surge in the Qingdao area under the impact of climate change. J. Ocean Univ. China 13 (4), 539–551.

Flather, R.A., 1994. A storm surge prediction model for the northern Bay of Bengal with application to the cyclone disaster in April 1991. J. Phys. Oceanogr. 24 (1), 172–190.

Flather, R.A., Smith, J.A., 1998. First estimates of changes in extreme storm surge elevations due to the doubling of CO2. Glob. Atmos. Ocean Syst. 6 (2), 193–208.

Fritz, H.M., Blount, C., Sokoloski, R., Singleton, J., Fuggle, A., McAdoo, B.G., et al., 2007. Hurricane Katrina storm surge distribution and field observations on the Mississippi Barrier Islands. Estuar. Coast Shelf Sci. 74 (1), 12–20.

Guan, F.C., Yu, B., Lin, S.Y., Xia, Z.W., 2000. A symmetrical typhoon wind field model in numerical simulation of storm surge in the South China Sea. Guangdong Meteorology 22 (1), 44–49 (In Chinese).

Guo, H.R., Jiao, W.H., Yang, Y.X., 2004. The systematic difference and its distribution between the 1985 national height datum and the global quasigeoid. Acta Geod. Cartogr. Sinica 33 (2), 100–104 (In Chinese).

Guo, Y., Zhang, J., Zhang, L., Shen, Y., 2009. Computational investigation of typhoon-induced storm surge in Hangzhou Bay, China. *Estuarine*. Coastal and Shelf Science 85 (4), 530–536.

Haigh, I.D., Wijeratne, E.M.S., MacPherson, L.R., Pattiaratchi, C.B., Mason, M.S., Crompton, R.P., George, S., 2014. Estimating present day extreme water level exceedance probabilities around the coastline of Australia: tides, extra-tropical storm surges and mean sea level. Clim. Dynam. 42 (1–2), 121–138.

Horsburgh, K.J., Wilson, C., 2007. Tide-surge interaction and its role in the distribution of surge residuals in the North Sea. J. Geophys. Res.: Oceans 112 (C8).

Irish, J.L., Resio, D.T., Ratcliff, J.J., 2008. The influence of storm size on hurricane surge. J. Phys. Oceanogr. 38 (9), 2003–2013.

Jarvis, A., Reuter, H.I., Nelson, A., Guevara, E., 2008. Hole-filled SRTM for the Globe Version 4. available from: the CGIAR-CSI SRTM 90m Database. http://srtm.csi.cgiar.org.

Jelesnianski, C.P., 1965. A numerical calculation of storm tides induced by a tropical storm impinging on a continental shelf. Mon. Weather Rev. 93, 343–358.

Jiang, G., Wu, Y., Zhu, S., Sha, W., 2003. Numerical simulation of typhoon wind field on Zhanjiang Port [J]. Mar. Forecasts 2, 41–48 (In Chinese).

Jiang, Z., Hua, F., Qu, P., 2008. A new scheme for adjusting the tropical cyclone parameters. Adv. Mar. Sci. 26 (1), 1 (In Chinese).

Jones, J.E., Davies, A.M., 1998. Storm surge computations for the Irish Sea using a three-dimensional numerical model including wave–current interaction. Continent. Shelf Res. 18 (2), 201–251.

Jones, J.E., Davies, A.M., 2009. Storm surge computations in estuarine and near-coastal regions: the Mersey estuary and Irish Sea area. Ocean Dynam. 59 (6), 1061–1076.

Katsman, C.A., Sterl, A., Beersma, J.J., Van den Brink, H.W., Church, J.A., Hazeleger, W., et al., 2011. Exploring high-end scenarios for local sea level rise to develop flood protection strategies for a low-lying delta—The Netherlands as an example. Climatic Change 109 (3–4), 617–645.

Li, J., Fang, W., Zhang, X., Cao, S., Yang, X., Liu, X., Sun, J., 2016. Similar tropical cyclone retrieval method for rapid potential storm surge and wave disaster loss assessment based on multiple hazard indicators. Mar. Sci. 40 (8), 49–60 (In Chinese).

Lowe, J.A., Gregory, J.M., Flather, R.A., 2001. Changes in the occurrence of storm surges around the United Kingdom under a future climate scenario using a dynamic storm surge model driven by the Hadley Centre climate models. Clim. Dynam. 18 (3), 179–188.

Luettich, R.A., Westerink, J.J., 2004. Formulation and Numerical Implementation of the 2D/3D ADCIRC Finite Element Model. pp. 74 version 44. XX.

Ma, J., Hu, J., 2004. Analysis and summary of storm surge in 2003 and their forecast. Mar. Forecasts 21 (2), 74–85 (In Chinese).

Olbert, A.I., Hartnett, M., 2010. Storms and surges in Irish coastal waters. Ocean Model. 34 (1), 50–62.

Pasquali, D., Di Risio, M., De Girolamo, P., 2015. A simplified real time method to forecast semi-enclosed basins storm surge. *Estuarine*. Coastal and Shelf Science 165, 61–69.

Pugh, D., 2004. Changing Sea Levels: Effects of Tides, Weather and Climate. Cambridge University Press.

Rahmstorf, S., 2007. A semi-empirical approach to projecting future sea-level rise. Science 315 (5810), 368–370.

Shen, J., Gong, W., 2009. Influence of model domain size, wind directions and Ekman transport on storm surge development inside the Chesapeake Bay: a case study of extratropical cyclone Ernesto, 2006. J. Mar. Syst. 75 (1), 198–215.

Shi, H., Huang, H., 2013. Comparative analysis of the storm surge between 1117 (Nesat) and 1119 (Nalgae). Mar. Forecasts 30 (2), 62–67.

Soloman, S., Qin, D.H., Manning, M., Alley, R.B., Berntsen, T., 2007. Climate Change 2007-The Physical Science Basis: Working Group I Contribution to the Fourth Assessment Report of the IPCC, vol. 4 Cambridge University Press.

Soontiens, N., Allen, S.E., Latornell, D., Le Souëf, K., Machuca, I., Paquin, J.P., et al., 2016. Storm surges in the Strait of Georgia simulated with a regional model. Atmos.-Ocean 54 (1), 1–21.

Vermeer, M., Rahmstorf, S., 2009. Global sea level linked to global temperature. Proc. Natl. Acad. Sci. Unit. States Am. 106 (51), 21527–21532.

Wang, X., Sun, B., Chen, Q., Ma, X., Huang, G., 2008. The analyzing and summarizing of the storm surge caused by typhoon NO.6 (Prapiroon) in 2006. Mar. Forecasts 25 (2), 99–105 (In Chinese).

Ying, Z., Wang, H., 1996. The relationship between fill-block engineering and tidal inlet system response in Zhanjiang Bay. Acta Scientlarum Naturalium Universitatis Sunyatseni 35 (6), 101–105 (In Chinese).

Ying, M., Zhang, W., Yu, H., Lu, X., Feng, J., Fan, Y., Chen, D., 2014. An overview of the China Meteorological Administration tropical cyclone database. J. Atmos. Ocean. Technol. 31 (2), 287–301.

Zhang, W., Huang, W., Zhu, S., 2009. Application of satellite remote sensing data to storm surge flooding calculation. Journal of PLA University of Science and Technology: Natural Science Edition 10 (5), 501–506 (In Chinese).

Zhang, K., Li, Y., Liu, H., Xu, H., Shen, J., 2013. Comparison of three methods for estimating the sea level rise effect on storm surge flooding. Climatic Change 118 (2), 487–500.